CHALMERS
UNIVERSITY OF TECHNOLOGY

Energy-Efficient Wheel Torque Distribution for Heavy Electric Vehicles with Adaptive Model Predictive Control and Control Allocation

Downloaded from: https://research.chalmers.se, 2025-11-25 08:25 UTC

Citation for the original published paper (version of record):
Janardhanan, S., Persson, J., Jonasson, M. et al (2025). Energy-Efficient Wheel Torque Distribution for Heavy Electric Vehicles with Adaptive Model
Predictive Control and Control Allocation. IEEE Open Journal of Vehicular Technology, 6: 2909-2924. http://dx.doi.org/10.1109/OJVT.2025.3619823

N.B. When citing this work, cite the original published paper.

© 2025 IEEE. Personal use of this material is permitted. Permission from IEEE must be obtained for all other uses, in any current or future media, including reprinting/republishing this material for advertising or promotional purposes, or reuse of any copyrighted component of this work in other works.

(article starts on next page)

IEEE Open Journal of Vehicular Technology

Received 23 September 2025; accepted 1 October 2025. Date of publication 9 October 2025;
date of current version 5 November 2025. The review of this article was coordinated by Editor Haiping Du.

Digital Object Identifier 10.1109/OJVT.2025.3619823

Energy-Efficient Wheel Torque Distribution for Heavy Electric Vehicles With Adaptive Model Predictive Control and Control Allocation

SACHIN JANARDHANAN [1,2], JONAS PERSSON [2], MATS JONASSON [1], BENGT JACOBSON [1], ESTEBAN R GELSO [2], AND LEON HENDERSON [1,2]

[1]Chalmers University of Technology, M building, Hörsalsvägen 7 A, 412 96 Gothenburg, Sweden
[2]Volvo Group Trucks Technology, Gropegårdsgatan 10, 417 15 Gothenburg, Sweden

CORRESPONDING AUTHOR: SACHIN JANARDHANAN (e-mail: sachin.janardhanan@chalmers.se).

This work was supported in part by the Swedish Energy agency under the Vehicle Research and Innovation Program (FFI) under Grant P2023-00590 and in part by the Volvo group.

ABSTRACT This paper proposes an energy efficient hierarchical wheel torque controller for a 4 × 4 heavy electric vehicle equipped with multiple electric drivetrains. The controller consists of two main components: a global force reference generator and a control allocator. The global force reference generator computes motion requests based on steering wheel angle and longitudinal acceleration inputs, while adhering to actuator and tire force constraints. For this purpose, a linear time-varying model predictive controller (LTV-MPC) is employed to minimize the squared errors in yaw rate and longitudinal acceleration over a short prediction horizon. Concurrently, the controller dynamically identifies safe operating limits based on current driving conditions. These limits are then used to adjust the state cost weights dynamically, thereby improving the effectiveness of the MPC cost function. The control allocator (CA) subsequently distributes the force demands from the global reference generator among the electric machines and friction brakes. This allocation process minimizes instantaneous power losses while respecting actuator and tire force constraints. To further enhance energy efficiency, the method leverages the heterogeneous nature of the electric machines by minimizing not only operational power losses but also idle losses (power losses at zero torque), ensuring safe vehicle operation. The proposed strategy is evaluated using a high-fidelity vehicle model under various driving scenarios, including low-friction surfaces and near-handling-limit conditions. Simulation results demonstrate that dynamically varying state cost weights in conjunction with safe operating limits significantly improves vehicle performance, enhances energy efficiency, and reduces driver effort.

INDEX TERMS Model predictive control, control allocation, electric vehicles, limit handling.

I. INTRODUCTION

The ongoing shift in the automotive industry toward electrification has significantly increased the market share of battery electric vehicles (BEVs), including heavy commercial vehicles [1]. Consequently, research efforts have largely focused on advancing battery technologies, enhancing the efficiency of propulsion systems, and optimizing energy management strategies to reduce the overall power consumption of electric vehicles (EVs), there by increasing driving range [2]. Within this context, extensive attention has been directed toward exploring various powertrain configurations and their corresponding control strategies, particularly in terms of their influence on both handling performance and energy efficiency [3], [4], [5].

Torque vectoring (TV) is one such method involving modulation of individual wheel torques to influence the vehicle's yaw moment and energy efficiency, offering a significant opportunity to enhance vehicle performance. Various TV control approaches have been proposed in the literature, [4], [5], [6], [7], [8], [9]. The TV control design is often divided into two parts: the yaw moment reference generator and the wheel torque distribution component [10], [11]. A

© 2025 The Authors. This work is licensed under a Creative Commons Attribution 4.0 License. For more information, see https://creativecommons.org/licenses/by/4.0/

hierarchical control structure can reduce the dimensionality of the optimization strategy and incur fewer computations. Recent TV control research on distributed drive electric vehicles has presented a range of control strategies and methods, each designed for different operational goals and road conditions. In [4] state-of-the-art control methods were compared and underlined the superiority of model predictive control (MPC) over alternatives like sliding mode control (SMC), proportional integral derivative (PID), and linear quadratic control (LQR). MPC is widely regarded as the most preferred control method due to its ability to handle multi-variable constraints and predict future vehicle states, enabling simultaneous optimization of stability and energy efficiency [4], [7], [12].

MPC-based TV strategies rely on simplified yet sufficiently accurate vehicle models to ensure real-time performance [7], [11], [13]. Nonlinear MPC (NMPC) is widely explored for torque vectoring in distributed drive electric vehicles due to its ability to handle complex nonlinear dynamics and constraints. However, its real-time implementation is often challenged by high computational demands. To address this, many studies propose simplified or reformulated NMPC approaches. Kang et al. [12] and Guo et.al [14] proposed fast iterative MPC schemes and control allocation strategies to enable real-time torque distribution while maintaining stability and energy efficiency. Parra et al. [13] and Guo et al. [15] incorporate nonlinear models and stability constraints but streamline formulations for practical execution. Yin et al. [16] emphasize online real-time MPC for independently driven axles through meta heuristic algorithms, while cooperative and multi-objective control frameworks proposed in [17]. Wang et al. [18] further simplify optimization problems into linear time varying (LTV) formulations to balance performance and computational feasibility, when dealing with more number of axles.

Tuning model predictive controller requires careful adjustment of several factors at the outset—namely, the prediction and control horizons, cost function weights, and constraints—which are all critical to achieving the desired system performance. Most studies focus primarily on tuning weights related to yaw rate and side slip angle limits, which are essential indicators of vehicle handling and lateral stability. Guo et al. [17] tune weights within a cooperative ARS and DYC framework to balance handling agility against lateral stability and energy consumption, where increasing stability weights constrains yaw rate and side slip excursions within safe bounds. Parra et al. [13] onsider weights associated with longitudinal and lateral tire forces to prevent tire saturation, indirectly affecting stability, but explicit longitudinal weight tuning remains relatively rare. Supervisory and Lyapunov-based NMPC strategies [19] [15] emphasize constraints on yaw rate and sideslip angles derived from vehicle-specific stability criteria to ensure safe operation near dynamic limits. Wang et al. [18] extend these tuning principles to multi-axle vehicles, balancing stability, handling, and actuator effort mainly through yaw rate and side slip constraints. Despite their importance, longitudinal weights are less frequently integrated explicitly, suggesting an opportunity for more comprehensive control designs that jointly address lateral and longitudinal dynamics.

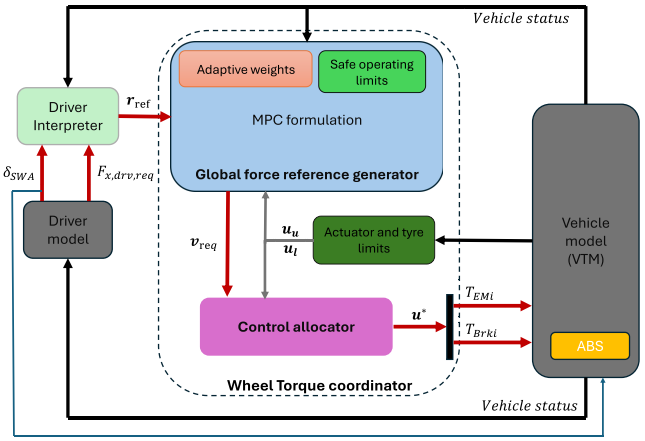

FIGURE 1. Overview and composition of the system under investigation.

Hence, in the present study, the following contributions to the literature gap are aimed:

- Formulation of an hierarchical and modular wheel torque coordination framework for an electric vehicle with multiple drivetrains using different type of electric machines. The framework employs a LTV-MPC and a control allocator.
- Model based approach to vary state cost weights and state limits of the LTV-MPC dynamically. Particularly, balancing the weights concerning longitudinal and lateral states are emphasized. State cost weights are specified using vehicle characteristic parameters with the aim to achieved modularity.
- Emphasizing the influence on the choice of tuning parameters in LTV-MPC and their impact of vehicle performance on low friction conditions for different use cases.

The remainder of this paper is organised as follows. In Section III the model predictive control oriented wheel torque coordinator is presented with detailed description and models of all the subsystems including the adaptive state cost varying method and safe operating limits. Next the validation of vehicle models used in this paper are highlighted in section IV. Finally, the results from simulations for the different use-cases are presented in section V and followed by conclusion in section VI.

II. SYSTEM OVERVIEW AND VEHICLE CONFIGURATION

A. OVERVIEW OF SYSTEM AND SIMULATION FRAMEWORK

The overall system used to investigate the wheel torque coordination strategy is presented in Fig. 1. The proposed system consists of the following:

- *Driver model* - which assists the vehicle to track the defined road curvature and reference speed. The outputs from the driver model are longitudinal force request and steering wheel angle request.

- *Driver interpreter* - which converts the driver model outputs to instantaneous targets (scalar values) for the controller, while observing the current vehicle states. The driver interpreter generates targets $\boldsymbol{r}_{\text{ref}}$ as in (1) using the requests from the driver model, namely the longitudinal force request $F_{x,\text{drv,req}}$ and steering wheel angle request δ_{f}.

$$\boldsymbol{r}_{\text{ref}} = \begin{bmatrix} a_{x,\text{ref}} & v_{x,\text{ref}} & \omega_{z,\text{ref}} & \beta_{\text{ref}} \end{bmatrix}^T \tag{1}$$

  In this paper, only the targets $a_{x,\text{ref}}$ the longitudinal acceleration and $\omega_{z,\text{ref}}$ the yaw rate reference in $\boldsymbol{r}_{\text{ref}}$ are actively tracked. To avoid tracking other targets, the reference longitudinal velocity request $v_{x,\text{ref}}$ and reference body side slip angle request β_{ref} are set to current longitudinal velocity and body side slip angle of vehicle respectively. Whereas the target values for the reference yaw rate $\omega_{z,\text{ref}}$ and longitudinal acceleration, $a_{x,\text{ref}}$ were achieved according to (2) and (3).

$$\omega_{z,\text{ref}} = \frac{v_x \cdot \delta_{\text{SWA}}}{k_{\text{steer}} \cdot (L_f + L_r + m \cdot K_u \cdot v_x^2)} \tag{2}$$

$$a_{x,\text{ref}} = \frac{F_{x,\text{drv,req}}}{m} \tag{3}$$

  With the aim of achieving a predictable vehicle behaviour for the driver, a steady-state yaw rate $\omega_{z,\text{ref}}$ was chosen as the reference. Thus, the vehicle should reach and operate in steady state as soon as possible when a disturbance is introduced. Additionally, it is also possible to emulate the neutral and understeered behaviour of the vehicle if required. However, with the possibility of TV, a neutral-steered vehicle, with understeer coefficient $K_u = 0$ is achievable and preferred in this study.
- *Wheel torque coordinator* - which processes driver interpreter requests and feedback of vehicle and actuator (electric machine and friction brake) states to generate optimal actuator requests. Consequently, the coordinated actuator requests are converted into wheel torque requests. An Anti-lock braking system (ABS) is also included to handle cases with infeasible wheel torque requests as a safety mechanism. The ABS shuts off the electric motors on the axle when active. During the active phase, it continuously allows more friction brake torque until the wheel either locks again or matches the desired torque of the driver. While this is not a model of ABS system used in mass produced vehicles, it provides satisfactory and accurate performance than simply letting locking of the wheels.
- *Vehicle model (VTM)* - which receives individual wheel torque requests and steering wheel angle request from wheel torque coordinator and drive model respectively, and generates desired the vehicle motion. The vehicle motion related states are simultaneously relayed back to the different subsystems to close the loop. A high-fidelity vehicle model developed in-house by Volvo Group Trucks Technology using the Volvo Transport Models library (VTM) was used in this study [20].

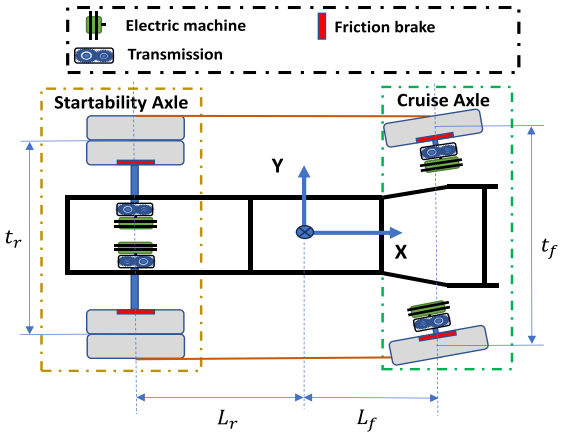

FIGURE 2. Vehicle configuration with cruise axle in the front and startability axle in the rear.

Throughout this paper the subscript $i = fl, fr, rl, rr$, is used to represent the wheel corners, where fl represents front axle left wheel, fr front axle right wheel, rl rear axle left wheel and rr rear axle right wheel. However, in case of single track models and related variables $i = f, r$ representing the front and rear wheels.

B. VEHICLE CONFIGURATION

The vehicle configuration chosen for this study is a 4x4 heavy duty tractor, with an individual electric drivetrain and friction brake on each wheel, as shown in the Fig. 2. The axles are organized into two main groups: the front axle group and the rear axle group. Additionally, they are also categorized based on different operating modes, allowing for flexible torque distribution and control strategies tailored to specific driving conditions or system configurations. Accordingly, in the Fig. 2, the front axle is configured as cruise axle (for cruise mode operation) and rear axle as startability axle (for startability and power mode operation in combination with the cruise axle) [21]. The electric machines (EMs) on the front axle are configured using a permanent magnet synchronous machine (PMSM) and that on the rear axle using induction machines (IM). The important parameters are highlighted in Table 1. For additional specifications and details of EM maps, readers are directed to explore [22].

III. WHEEL TORQUE COORDINATION CONTROLLER

The wheel torque coordination controller, functions by translating the driver's input requests into individual wheel torques, utilizing feedback from the vehicle's motion and actuator states as shown in Fig. 1. To maintain safe operation of the vehicle system, constraints are applied to both the vehicle states and actuator inputs. The wheel torque coordination controller is hierarchically structured and consists of two main components: a global force reference generator and a control allocator. The global force reference generator aims to define a safe motion target reference for the control allocator. The control allocator then translates these motion requests into

TABLE 1. Table of Parameters Describing the Vehicle

Variable	Description
ω_z	Angular yaw velocity of vehicle (rad/s)
β	Body slip angle (rad)
$F_{z,i}$	Vertical force on tyre (N)
δ_f	Steering angle at the wheel (rad)
$\omega_{\text{whl}i}$	Angular wheel speed (rad/s)
v_x	Longitudinal velocity of vehicle (m/s)
a_x	Longitudinal vehicle acceleration at CoG (m/s^2)
a_y	Lateral vehicle acceleration at CoG (m/s^2)
θ_z	Vehicle yaw angle (rad)
T_i	Wheel torque request (Nm)
$T_{\text{req,EM}i}$	Electric machine torque request (Nm)
$T_{\text{req,Brk}i}$	Friction brake torque request (Nm)
M_z	Vehicle yaw moment (Nm)
$P_{\text{loss,EM}i}$	Power losses of electric machine (kW)
$P_{\text{loss,Brk}i}$	Power losses of friction brake (kW)
$T_{\text{lim,tyre}i}$	Wheel torque limit (Nm)
$T_{\text{lim,EM}i}$	Electric machine torque limit for a given speed (Nm)
$T_{\text{lim,Brk}i}$	Friction brake torque limit (Nm)

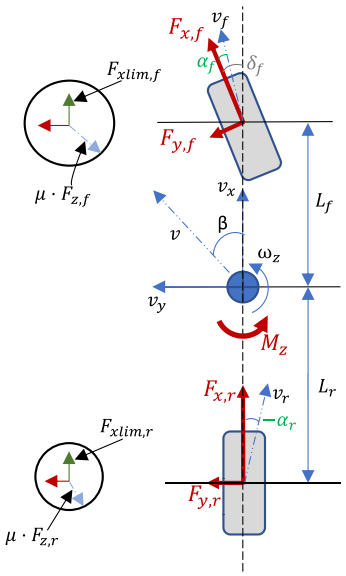

FIGURE 3. Single track vehicle model used in the controller with representation of friction ellipse based tyre force limitation.

individual wheel torques by coordinating the actuator inputs while minimizing the energy consumption. A hierarchical structure was chosen in study with the aim to manage the complexity of solving the problem in real-time and to facilitate scalability and flexibility for different vehicle configurations.

A. GLOBAL FORCE REFERENCE GENERATOR

The global force reference generator receives input from the driver interpreter while monitoring the vehicle state, actuator status, and system constraints. It then generates a motion request vector, $\boldsymbol{v}_{\text{req}}$ consisting of two components:

$$\boldsymbol{v}_{\text{req}} = \begin{bmatrix} F_{x,\text{req}} & M_{z,\text{req}} \end{bmatrix}^T \tag{4}$$

Here, $F_{x,\text{req}}$ represents the global longitudinal force, and $M_{z,\text{req}}$ denotes the yaw moment request respectively. To generate these global force requests, the global force reference generator employs a Model Predictive Control (MPC) strategy. MPC was selected as the preferred control method due to several key advantages, including:

- *Predictive Capability:* MPC can anticipate future system behaviour based on a dynamic model, allowing it to plan control actions proactively.
- *Constraint Handling:* It can explicitly incorporate constraints on states and inputs, ensuring safe and feasible control decisions.
- *Multi-variable Optimization:* MPC can manage multiple inputs and outputs simultaneously, making it well-suited for complex systems like vehicle dynamics.
- *Adaptability:* It allows the integration of real-time feedback to adjust control strategies dynamically as the vehicle and environmental conditions change.

The different components within the global force generator are presented in the following subsections.

TABLE 2. Table of Variables

Parameter	Denotation	Unit	Value
Track width, front	t_f	m	2.09
Track width, rear	t_r	m	1.85
Max continuous power, PMSM	$P_{max,crs}$	kW	200
Gear ratio, Cruise axle	gr_{crs}	-	4.5
Max continuous power, IM	$P_{max,stb}$	kW	180
Gear ratio, Startability axle	gr_{stb}	-	26
Gravity constant	g	m/s^2	9.81
Mass	m	kg	6830
Rolling resistance coefficient	c_r	N/N	0.008
Air density	ρ	kg/m^3	1.2
Air resistance coefficient	C_d	-	0.59
Cornering stiffness, front	C_f	kN/rad	283
Cornering stiffness, rear	C_r	kN/rad	120
Frontal area	A_f	m^2	10
Wheel base	L	m	3.8
Distance, CoG to front axle	L_f	m	1.08
Distance, CoG to rear axle	L_r	m	2.72
Wheel radius	r_w	m	0.47
Yaw inertia	I_{zz}	kg m^2	26146
Steering gear ratio	k_{steer}	-	20

1) VEHICLE MODEL USED BY THE MODEL PREDICTIVE CONTROLLER

To generate $\boldsymbol{v}_{\text{req}}$ the global force reference generator uses a transient single-track vehicle model, as seen in Fig. 3, with 3 degrees of freedom. The model is also extended to include additional yaw moment from different longitudinal tyre forces on left and right side. Table 2 describes the important variables used in the model.

The state dynamics formulation of the vehicle model using state vector $\boldsymbol{x}$ and control input $\boldsymbol{u}_{\text{mpc}}$ is shown in (5).

$$\dot{\boldsymbol{x}}(t_s) = f(\boldsymbol{x}(t_s), \boldsymbol{u}_{\text{mpc}}(t_s)) \tag{5}$$

$$\boldsymbol{x} = \begin{bmatrix} \dot{v}_x \; v_x \; \omega_z \; \beta \end{bmatrix}^T, \quad \boldsymbol{u}_{\text{mpc}} = \begin{bmatrix} T_{fl} \; T_{fr} \; T_{rl} \; T_{rr} \end{bmatrix}^T$$

An additional state $\dot{v}_x$ is added to the state vector to facilitate the model to receive acceleration requests instead of velocity requests. The states of the vehicle plant are fed back to controller serving as the initial conditions $\boldsymbol{x}_{\text{init}}$ for the predictions performed using the model defined in (5).

The vehicle model used in the controller is based on a non-linear tire model without involving the effect of combined slip [23].

$$F_{y,i} = \mu \cdot F_{z,i} \tanh\left(\frac{C_i \cdot \alpha_i}{\mu \cdot F_{z,i}}\right) \tag{6}$$

In order to retain non-linear tire characteristic while preserving the convexity of the optimization problem, the tyre model is linearized around the operating point, i.e., the current side slip angle, at every iteration of the control algorithm. The localised cornering stiffness around current slip angle is obtained through $\tilde{C}_i = (\frac{F_{y,i}}{\alpha_i})|_{\alpha_i(t_s)}$.

The force and moment balance equations governing the degree of freedom of the vehicle model, using the localised cornering stiffness, are shown in (7) - (10). In order to avoid introducing non-linear relationships in the model, the longitudinal velocity value at each iteration of the control algorithm, $v_x(t_s)$, was used for the entire MPC horizon. Thus $v_x(t_s)$, which remains constant is added as a parameter during the MPC iterations. This is expected not to cause significant deviation between the model and actual vehicle states because of slower dynamics for the heavy vehicles. To implement the torque vectoring feature to the controller model, additional information on how the torque on each wheel affects the vehicle yaw motion is added equation (7).

- Yaw moment balance

$$\begin{aligned} \dot{\omega}_z = & -\left(\frac{L_f \cdot \tilde{C}_f - L_r \cdot \tilde{C}_r}{I_{zz}}\right)\beta + \left(\frac{L_f \cdot \tilde{C}_f}{I_{zz}}\right)\delta_f \\ & - \left(\frac{L_f^2 \cdot \tilde{C}_f - L_r^2 \cdot \tilde{C}_r}{I_{zz} \cdot v_x(t_s)}\right)\omega_z \\ & + \frac{\begin{bmatrix} -t_f & t_f & -t_r & t_r \end{bmatrix}}{(2\, I_{zz} \cdot r_w)} \boldsymbol{u}_{\text{mpc}} \end{aligned} \tag{7}$$

- Lateral force balance

$$\begin{aligned} \dot{\beta} = & -\left(\frac{\tilde{C}_f + \tilde{C}_r}{m \cdot v_x(t_s)}\right)\beta + \left(\frac{\tilde{C}_f}{m \cdot v_x(t_s)}\right)\delta_f \\ & + \left(\frac{-L_f \cdot \tilde{C}_f + L_r \cdot \tilde{C}_r}{m \cdot v_x^2(t_s)} - 1\right)\omega_z \end{aligned} \tag{8}$$

- Longitudinal force balance

$$\begin{aligned} \dot{v}_x = & \; \omega_z \cdot v_y + \frac{(T_{fr} + T_{fl} + T_{rl} + T_{rr})}{r_w \cdot m} - \frac{C_r \cdot F_z}{m} \\ & - \frac{1}{m}\left(\frac{1}{2}\rho \cdot C_d \cdot A_f \cdot v_x^2(t_s) + sin(\theta) \cdot m \cdot g\right) \end{aligned} \tag{9}$$

Additionally, a linear state space model that updates the acceleration must calculate the rate of change in the acceleration. To realise this, finite difference approximation was used to approximate the rate of change between each horizon step k. This allows acceleration requests in addition to velocity requests.

$$\ddot{v}_x = \frac{\dot{v}_x[k+1] - \dot{v}_x[k]}{T_{s,\text{mpc}}} \tag{10}$$

The control-oriented model is further simplified not by two assumptions: (i) longitudinal and lateral tire forces are decoupled, and (ii) wheel dynamics are neglected. Although these assumptions reduce model complexity, the neglected dynamics are incorporated in the controller design. In particular, the maximum lateral force is related to the longitudinal force via the friction ellipse, ensuring adherence to tire limits.

Lateral tire forces are computed from vehicle feedback based on estimated axle loads and lateral acceleration, and are assumed constant over the prediction horizon:

$$F_{y,i} = \frac{F_{z,i}(t_s) \cdot a_y(t_s)}{g} \tag{11}$$

Neglecting wheel inertia and slip, the longitudinal tire force is expressed as:

$$\begin{aligned} F_{x,i} = \mu \cdot F_{z,i}(t_s) = \frac{T_i}{r_w} \\ \text{where} \mu \text{is the friction coefficient} \end{aligned} \tag{12}$$

To account for the neglected wheel dynamics, the MPC formulation constrains the maximum wheel torque, preventing excessive wheel accelerations.

Under these linearized assumptions and ignoring tire slip, the combined tire force limit is given by:

$$\mu F_{z,i} = \sqrt{F_{x,i}^2 + F_{y,i}^2} \tag{13}$$

To enhance robustness against tire model uncertainties and unmodeled dynamics, a safety factor n_{conf} is applied to the longitudinal force limit:

$$\begin{aligned} F_{x\text{lim,tyre}i} = n_{\text{conf}} \cdot \sqrt{(\mu \cdot F_{z,i}(t_s))^2 - F_{y,i}^2} \\ \text{where,} n_{\text{conf}} = 0.9 \end{aligned} \tag{14}$$

In the remainder of this paper, $F_{x\text{lim,tyre}i}$ is understood to include this safety factor unless otherwise stated.

Finally, this limit is converted into wheel torque constraints for the controller:

$$T_{\text{lim,tyre}i} = F_{x\text{lim,tyre}i} \cdot r_w \tag{15}$$

This formulation allows the MPC to enforce physically feasible tire forces while maintaining computational simplicity in the control-oriented model.

2) ACTUATOR AND TYRE FORCE OPERATING LIMITS

The wheel torque limits are restricted due to the limitation of actuators to provide the requested torque. Additionally, the dynamics of the actuators also restrict the total limit for the current state and is introduced using linear dynamics with a time constant $\tau_{\mathrm{EM}i}$ as in (16).

$$\begin{aligned} T_{\mathrm{EM}i} &= \left(T_{\mathrm{req,EM}i}(t_s) - \tau_{\mathrm{EM}i}\frac{T_{\mathrm{req,EM}i}(t_s)}{t}\right) \\ T_{\mathrm{lim,max,EM}i} &= \min(T_{\mathrm{lim,EM}i}, T_{\mathrm{EM}i}) \\ T_{\mathrm{lim,min,EM}i} &= \max(-T_{\mathrm{lim,EM}i}, T_{\mathrm{EM}i}) \end{aligned} \tag{16}$$

The torque limits, $T_{\mathrm{lim,EM}i}$ of the EMs in this study are obtained for a given operating speed using a look-up table as proposed in [22] and are assumed be constant for entire prediction horizon.

For friction brakes, the maximum torque limits $T_{\mathrm{lim,Brk}i}$ are set to constant values and assumed to provide the desired torque without any saturation. Thus, as in (16), the torque limits for friction brakes are given as:

$$\begin{aligned} T_{\mathrm{Brk}i} &= \left(T_{\mathrm{req,Brk}i}(t_s) - \tau_{\mathrm{Brk}i}\frac{T_{\mathrm{req,Brki}}(t_s)}{t}\right) \\ T_{\mathrm{lim,min,Brk}i} &= \max(-T_{\mathrm{lim,Brk}i}, T_{\mathrm{Brk}i}) \\ T_{\mathrm{lim,max,Brk}i} &= 0 \end{aligned} \tag{17}$$

The actuator limits and the tyre force limits are evaluated at each instant to avoid sending actuator requests more than the wheel force limit capabilities and the actuator capabilities. The minimum $\boldsymbol{u_l}$ and maximum $\boldsymbol{u_u}$, torque limits ensure that the actuator operating limits and the available friction limit are not violated.

$$\boldsymbol{u_u} = \begin{bmatrix} T_{\mathrm{max,EM}i} \\ \vdots \\ T_{\mathrm{max,Brk}i} \\ \vdots \end{bmatrix} \quad \boldsymbol{u_l} = \begin{bmatrix} T_{\mathrm{min,EM}i} \\ \vdots \\ T_{\mathrm{min,Brk}i} \\ \vdots \end{bmatrix}$$

$$\begin{aligned} T_{\mathrm{max,EM}i} &= \min(T_{\mathrm{lim,max,EM}i}, T_{\mathrm{lim,tyre}i}) \\ T_{\mathrm{min,EM}i} &= \max(T_{\mathrm{lim,min,EM}i}, -T_{\mathrm{lim,tyre}i}) \\ T_{\mathrm{max,Brki}} &= \min(T_{\mathrm{lim,max,Brk}i}, T_{\mathrm{lim,tyre}i}) \\ T_{\mathrm{min,Brki}} &= \max(T_{\mathrm{lim,min,Brk}i}, -T_{\mathrm{lim,tyre}i}) \end{aligned}$$

3) SAFE OPERATING LIMITS OF VEHICLE MOTION

In order to define safe vehicle operation, it is also necessary to set limits on the vehicle states in addition to the limits of actuators and tyre forces. The development of the vehicle states in $\boldsymbol{x}$ are observed using the simplified model defined in (5) for the prediction horizon.

The state limits are defined using the relations defined in [24] which are adapted as the following :

- Yaw rate limits:

$$\omega_{z,\max} = \frac{\mu g}{v_x(t_s)}, \quad \omega_{z,\min} = -\frac{\mu g}{v_x(t_s)} \tag{18}$$

- Side slip limits:

$$\begin{aligned} \beta_{\max} = \min\Bigg(& (tan(\alpha_{f,max} + \delta_f(t_s)) - \frac{L_f\omega_z(t_s)}{v_x(t_s)}, \\ & tan(\alpha_{r,max}) + \frac{L_r\omega_z(t_s)}{v_x(t_s)}\Bigg) \end{aligned} \tag{19}$$

$$\begin{aligned} \beta_{\min} = \max\Bigg(& (tan(-\alpha_{f,max} + \delta_f(t_s)) - \frac{L_f\omega_z(t_s)}{v_x(t_s)}, \\ & -tan(\alpha_{r,max}) + \frac{L_r\omega_z(t_s)}{v_x(t_s)}\Bigg) \end{aligned}$$

$$\text{where,} \alpha_{r,max} = \arctan\frac{4\mu F_{z,r}}{C_r}, \alpha_{f,max} = \arctan\frac{4\mu F_{z,f}}{C_f} \tag{20}$$

- Longitudinal acceleration and velocity limits:

$$\begin{aligned} a_{x,\max} &= \mu g, \quad a_{x,\min} = -\mu g \\ v_{x,\max} &= 25m/s, \quad v_{x,\min} = -10m/s \end{aligned}$$

The velocity limits here are chosen to represent the maximum forward and reversing speed of heavy vehicles on European motorways.

The state limits are then accumulated to be used as constraints in the optimization problem using $\boldsymbol{r}_{\min}$ and $\boldsymbol{r}_{\max}$.

$$\begin{aligned} \boldsymbol{r}_{\min} &= [a_{x,\min}, v_{x,\min}, \omega_{z,\min}, \beta_{\min}] \\ \boldsymbol{r}_{\max} &= [a_{x,\max}, v_{x,\max}, \omega_{z,\max}, \beta_{\max}] \end{aligned}$$

4) MPC OPTIMIZATION PROBLEM FORMULATION

The goal of the MPC is to optimize the future control actions, by minimising the square of error between the target and reference vehicle states (21), while respecting the vehicle, tyre, and actuator operating limits. The results from the optimization are a sequence of optimal control actions, over the prediction horizon, from which the first control action is selected.

$$\boldsymbol{e_x}(t_s) = \boldsymbol{x}(t_s) - \boldsymbol{r}_{\mathrm{ref}}(t_s) = \begin{bmatrix} \dot{v}_x \\ v_x \\ \omega_z \\ \beta \end{bmatrix} - \begin{bmatrix} a_{x,\mathrm{ref}} \\ v_{x,\mathrm{ref}} \\ \omega_{z,\mathrm{ref}} \\ \beta_{\mathrm{ref}} \end{bmatrix} \tag{21}$$

To formulate the stated objective, the single-track vehicle model in (5) is used to predict the motion ahead and compared with the predicted motion states of vehicle plant over a finite horizon N, at each simulation sample t_s. As only the vehicle states and reference states at t_s are used for the predictions, they remain static over the prediction horizon. This approach leads to acceptable results only in steady state operating conditions or extremely short prediction horizons. Hence, to introduce agile reference tracking, the reference

$\omega_{z,\text{ref}}$ is updated across horizon using first-order taylor expansion, using drivatives to predict future reference values. The predicted yaw rate at a predicted time instance $kT_{s,\text{mpc}}$, where k is a particular iteration step, is expressed as the following:

$$\omega_{z,\text{ref}}(k \cdot T_{s,\text{mpc}}) = \omega_{z,\text{ref}}(t_s) + \dot{\omega}_{z,\text{ref}}(t_s) k T_{s,\text{mpc}} \tag{22}$$

The derivatives of $\omega_{z,\text{ref}}$ are found using Savitzky-Golay filter. The choice of the order of the filter is motivated from the results in [22]. This method can be used to update other reference states (only two states are actively tracked) but is limited to $\omega_{z,\text{ref}}$ in this study.

Taking the above mentioned considerations into account, along with the constraints on actuators, states, and tire forces, the optimization problem is formally defined as follows:

$$\begin{aligned} \boldsymbol{u}^*_{\text{mpc}} = \min_{\boldsymbol{u}_{\text{mpc}}} \Bigg(& \sum_{k=1}^{\frac{N}{T_{s,\text{mpc}}}} \boldsymbol{e_x}(k) Q(k) \boldsymbol{e_x}(k)^T \\ & + \sum_{k=1}^{N-1} \boldsymbol{u}_{\text{mpc}}(k) R(k) \boldsymbol{u}^T_{\text{mpc}}(k) \Bigg) \end{aligned}$$

$$\begin{aligned} & \text{s.t. } \boldsymbol{x}(k+1) = f_d(\boldsymbol{x}(t), u(t)), \boldsymbol{x}(0) = \boldsymbol{x}_{\text{init}} \\ & \boldsymbol{u_l}(k) \le \boldsymbol{u}_{\text{mpc}}(k) \le \boldsymbol{u_u}(k), \quad k = 1, \ldots, N-1 \\ & \boldsymbol{r}_{\min}(k) \le \boldsymbol{r}_{\text{ref}}(k) \le \boldsymbol{r}_{\max}(k) \end{aligned} \tag{23}$$

where f_d is a discretized model of (5), Q and R are state and control costs weights.

The optimal outputs from the optimization are wheel torques which are used to achieve the desired vehicle motion. Since, the aim of the global force generator is to produce the global force requests, the wheel torques from optimization are recalculated as $F_{x,req}$ and $M_{z,req}$ as shown in (24).

$$\begin{bmatrix} F_{x,\text{req}} \\ M_{z,\text{req}} \end{bmatrix} = \begin{bmatrix} \frac{1}{r_w} & \frac{1}{r_w} & \frac{1}{r_w} & \frac{1}{r_w} \\ -\frac{t_f}{2\,r_w} & \frac{t_f}{2\,r_w} & -\frac{t_r}{2\,r_w} & \frac{t_r}{2\,r_w} \end{bmatrix} \boldsymbol{u}^*_{\text{mpc}} \tag{24}$$

The problem formulation in (23) is converted into a constrained quadratic problem formulation and solved using the batch approach.

$$\begin{aligned} \min_{z} \quad & \frac{1}{2} \mathbf{z}^\top H_{\text{mpc}} \mathbf{z} \\ \text{s.t.} \quad & A_{\text{eq}} \cdot \mathbf{z} = b_{\text{eq}} \\ & A_{\text{in}} \cdot \mathbf{z} \le b_{\text{in}} \end{aligned} \tag{25}$$

The MPC algorithm is implemented and solved using the *mpcInteriorPoint* solver available in MATLAB. The motivation of choosing the predictive controller parameters defined in Table 3 is briefly discussed in [22].

TABLE 3. Table of Parameters Used in the Model Predictive Controller

Parameter	Description	Time s
$T_{s,\text{mpc}}$	Horizon time step	0.1
N	Prediction horizon	1
T_{mpc}	Execution period	0.02

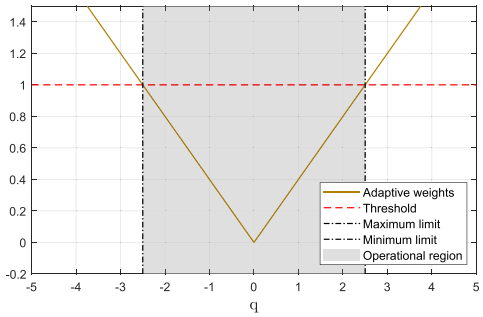

FIGURE 4. Example of evaluating adaptive weight described in (26) and (27).

5) OPERATING CONDITION-BASED TUNING OF CONTROL OBJECTIVES

The performance of the MPC described in section is highly dependent on several tuning parameters like step time, prediction horizon, state limits, and weights in the MPC cost function. Selecting these parameters is generally a difficult task because of their effect on closed-loop performance is not straightforward to predict.

In this study, an adaptive algorithm is presented which varies state cost weights depending on the current vehicle state, driver input, vehicle parameters and state limits. In this algorithm the state limits and current vehicle state are used to set weights for the cost function terms. To have uniform correlation in balancing the weights between different objectives, the weights are normalized and then scaled using vehicle parameters and variables. The normalized weights, within the range $0-1$ and their relations are defined as follows:

- Yaw rate tracking adaptive weight

$$w_{sc,\omega_z} = \begin{cases} 1 - \left(\frac{\omega_{z,\max} - \omega_{z,\text{ref}}}{\omega_{z,\max}} \right), & \text{if } \omega_{z,\text{ref}} \ge 0 \\ 1 - \left(\frac{\omega_{z,\min} - \omega_{z,\text{ref}}}{\omega_{z,\min}} \right) \end{cases} \tag{26}$$

- Body side slip tracking adaptive weight

$$w_{sc,\beta} = \begin{cases} 1 - \left(\frac{\beta_{\max} - \beta_{\text{ref}}}{\beta_{\max}} \right), & \text{if } \beta_{\text{ref}} \ge 0 \\ 1 - \left(\frac{\beta_{\min} - \beta_{\text{ref}}}{\beta_{\min}} \right) \end{cases} \tag{27}$$

- Longitudinal acceleration and velocity tracking adaptive weight

$$w_{sc,a_x} = w_{sc,v_x} = 1 - \max(w_{sc,\beta}, w_{sc,\omega_z}) \tag{28}$$

Fig. 4 illustrates the approach to evaluate the expressions in (26) and (27), using an independent variable q with a defined range of values.

Additionally, a linear relation is established between longitudinal and lateral motion related weights. The principle is to reduce longitudinal weights when the lateral vehicle states approach the state limits. In such cases, the lateral motion related state cost weights increases linearly depending on difference between vehicle states and limits. Similarly, when operating far from the lateral stability limits, higher weights are set for the longitudinal state cost weights. Here, only simple relations are established as a proof of concept, for a certain vehicle configuration and load condition, which can be further extended using complex relations. Related concepts are also proposed in [13], [19].

These normalized adaptive weights are then scaled before introducing into the optimization problem using vehicle parameters. This approach make this algorithm modular, especially to handle different and varying operating condition of heavy commerical vehicles.

$$Q = \left(\frac{mg}{2}\right)^2 \text{diag}\left[w_{sc,a_x}, w_{sc,a_x}, \left(\frac{4I_{zz}^2}{m^2}\right) w_{sc,\omega_z}, \frac{4w_{sc,\beta}}{g^2}\right] \tag{29}$$

B. CONTROL ALLOCATOR

1) POWER LOSS MINIMIZATION

The motion request $\boldsymbol{v}_{\text{req}}$ is distributed to each wheel through the combination of EM and friction brake torques by the control allocator. The control allocator achieves this task by solving an optimisation problem with the objective of minimising the power losses of the actuators instantaneously while achieving the requested $\boldsymbol{v}_{\text{req}}$ [21]. Note that, $\boldsymbol{v}_{\text{req}}$ also includes the yaw moment request in addition to the longitudinal force request, when compared to [21], that is to be mapped as individual actuator torque requests. The power losses of the EMs are expressed as a second-degree polynomial, extracted using regression of the power loss maps, approximating the power loss as a function torque as shown in (30). The EM speed dependent parameters $c_{2,\text{EM}i}$, $c_{1,\text{EM}i}$, and c_0, are used to fit the power loss measurement data for the specific EM.

$$P_{\text{loss,EM}i} = T_{\text{req,EM}i}^2 \cdot c_{2,\text{EM}i} + T_{\text{req,EM}i} \cdot c_{1,\text{EM}i} + c_{0,\text{EM}i} \tag{30}$$

Fig. 5, shows the regressed curve fit parameters for the EMs and their accuracy for a particular vehicle speed. The R^2 fitting accuracy of both the EMs using (30) are also seen to be greater than 0.97 for the entire operating range.

Likewise, the losses from the friction brakes are approximated using a linear relation of the wheel power as:

$$P_{\text{lossBrk}i} = -T_{\text{Brk}i} \cdot \omega_{\text{whl}i} \tag{31}$$

Consequently, the torque allocation to each actuator is obtained by solving an optimisation problem including the operating limits of actuators and tyres $\boldsymbol{u_l}$ and $\boldsymbol{u_u}$ used in the MPC formulation at each sampling instant as shown below:

$$\boldsymbol{u}^* = \min_{\boldsymbol{u}} \left(\sum_{j=1}^{n} P_{\text{loss,EM}i} + \sum_{j=1}^{n} P_{\text{loss,Brk}i} \right)$$

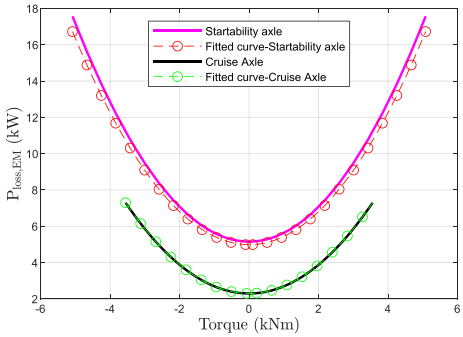

FIGURE 5. Power loss of electric machine with their quadratic approximation as a function of wheel torque for a vehicle speed of 60 km/h. The curve fit parameters for the quadratic approximations are: Cruise axle EM : $C_{2,EM1} = 0.0080$, $C_{1,EM1} = 2.03e^{-}16$, $C_{0,EM1} = 2297$ giving an R^2 fit of 1; Startability axle EM - $a_{stb} = 0.3072$, $b_{stb} = 8.26e^{-}16$, $c_{stb} = 4982$ giving an R^2 fit of 0.9886.

$$\text{s.t. } B \cdot \boldsymbol{u} = \boldsymbol{v}_{\text{req}}$$
$$\boldsymbol{u_l} \leq \boldsymbol{u} \leq \boldsymbol{u_u}$$
$$B = 1/r_w \cdot \begin{bmatrix} gr_{\text{crs}} & -\frac{gr_{\text{crs}} \cdot t_f}{2} \\ gr_{\text{crs}} & \frac{gr_{\text{crs}} \cdot t_f}{2} \\ gr_{\text{stb}} & -\frac{gr_{\text{stb}} \cdot t_f}{2} \\ gr_{\text{stb}} & \frac{gr_{\text{stb}} \cdot t_f}{2} \\ 1 & -\frac{t_f}{2} \\ 1 & \frac{t_f}{2} \\ 1 & -\frac{t_f}{2} \\ 1 & \frac{t_f}{2} \end{bmatrix}^T \tag{32}$$

A detailed description of the optimisation problem and the operating limits is presented in [22]. The optimisation problem in (32) is solved at each instant as a constrained quadratic programming (QP) problem and can therefore be reformulated into a standard form as follows:

$$\min_{\boldsymbol{u}} \quad \frac{1}{2}\boldsymbol{u}^T H \boldsymbol{u} + g^T \boldsymbol{u}$$
$$\text{s.t. } B \cdot \boldsymbol{u} = \boldsymbol{v}$$
$$\boldsymbol{u_l} \leq \boldsymbol{u} \leq \boldsymbol{u_u}$$

where,

$$H = 2 \cdot \begin{bmatrix} c_{2,\text{EM1}} & 0 & \dots & \dots & \dots & 0 \\ 0 & \ddots & 0 & \dots & \dots & \vdots \\ \vdots & \dots & c_{2,\text{EM}i} & \dots & \dots & \vdots \\ \vdots & \dots & \dots & a_{\text{Brk1}} & \dots & \vdots \\ \vdots & \dots & \dots & \dots & \ddots & 0 \\ 0 & \dots & \dots & \dots & 0 & a_{\text{Brk}i} \end{bmatrix}$$

$$g^T = \begin{bmatrix} c_{1,\text{EM1}}, \dots, c_{1,\text{EM}i}, -\omega_{\text{whl1}}, \dots, -\omega_{\text{whl}i} \end{bmatrix} \tag{33}$$

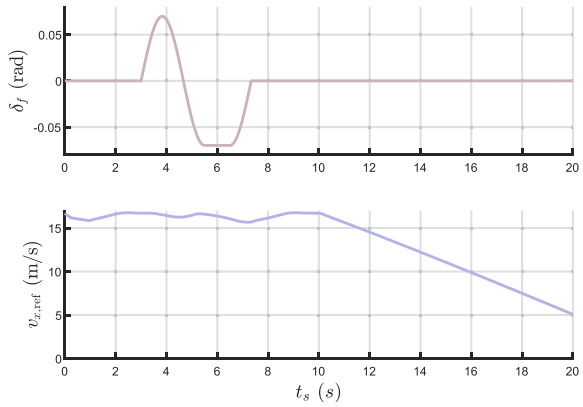

FIGURE 6. Sine with dwell manoeuvre steering wheel input at 16.67m/s followed by high deceleration braking at $\mu = 0.3$.

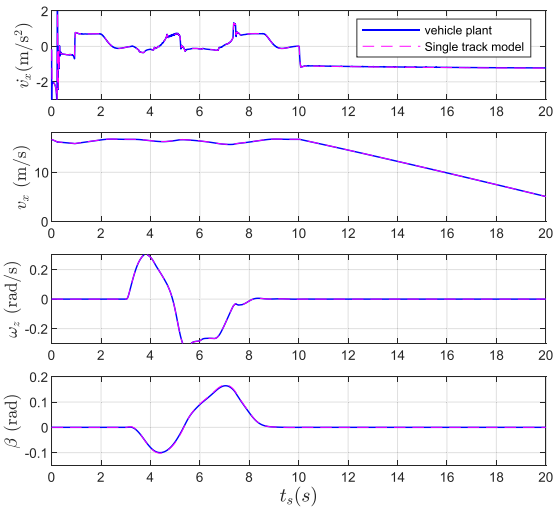

FIGURE 7. Comparison of states from the vehicle plant and the single track model used in the controller for the predictions.

where $a_{\mathrm{Brk}i}$ is a small value introduced to ensure that H is positive definite. The QP problem is implemented and solved using the $active-set$ solver available in MATLAB.

2) POWER LOSS MINIMIZATION INCLUDING IDLE LOSSES

Another efficient method to minimise power losses is to reduce the idle losses by completely electrically switching off the EMs as shown in previous studies [25]. The chosen vehicle configuration with IM on the startability axle facilitates such a feature, by requesting zero torque, due to its inherent operational characteristics (self-starting principle which avoid usage of a clutch). The idle losses represented by the parameter $c_{0,\mathrm{EM}i}$ is usually not involved in the standard QP formulation and hence needs special consideration. Such a implementation using logical statements is presented in [26]. Alternatively, the idle losses can also be represented by solving a QP problem with the entries in B corresponding to startability axle EM set to zero. Thus two QP problems are solved in parallel. The solution providing the minimal power loss is selected as the optimal solution. However, when the solution is feasible with the case including idle losses a decision to switch to the power loss minimisation case using all the machines is taken. To avoid continuous switching between the two solutions a time delay of 5 s is used to prioritise the power loss minimisation case with the EMs on both the axles active. This method is implemented and further evaluated in Section V.

IV. MODEL VERIFICATION

A. CONTROLLER BASED VEHICLE MODEL

In order to assess and verify the effectiveness of MPC controller the performance of the single track vehicle model used for predictions is verified. This is verified by simulating a open-loop test case of sine-with dwell manoeuvre according ISO 18375:2016 standard and braking at the end of the manouevre as shown in the Fig. 6.

The goal here is check how large are the errors between the single track model and vehicle plant model. As seen in the Fig. 7, the vehicle model in the controller tracks the vehicle plant motion with acceptable precision. A small tracking error in the longitudinal acceleration state during the transient motion which is expected due to lack longitudinal load transfer. Additionally, an error in the order of ± 0.002 rad is observed in the body slip angle, which is considered negligible, especially when driving aggressively in low friction conditions. The results also confirm that the numerical derivative used in (9), to approximate the longitudinal acceleration, is well within the acceptable range of error and no sign of delay or amplification error is seen. Hence, it can be confirmed that the controller based vehicle model is well suited for the application.

B. VEHICLE PLANT MODEL

Verification against real vehicle test data was conducted to ensure the accuracy and reliability of the vehicle plant and driver model. The data was recorded for a 4x2 electric tractor using brake in curve tests done on packed snow and without the wheel torque coordination controller. In contrast to the test conditions, the vehicle plant model reconfigured to be a rear-axle-driven vehicle, was simulated with the wheel torque coordination controller. The driver input from the recorded data is then fed into the simulation model using the controller with Q, $\boldsymbol{r}_{\max}$ and $\boldsymbol{r}_{\min}$ set according to Cfg-3 in Table 4. The signals, namely, the initial vehicle speed, steering wheel angle, and requested longitudinal acceleration are replayed and the output of the simulation model is compared to the real vehicle test measurements as shown in Fig. 8. As seen in Fig. 8, the simulation results and the measurement have similar trends, except for a slight deviations. Such a behaviour is expected due to the influence of the controller, simplified modelling of the actuator dynamics, and tyre-road friction contact. Moreover, these deviations in the simulation model are considered acceptable as the goal was to validate the dynamic performance of the vehicle model on low friction conditions. Consequently, the simulation model is adapted to

TABLE 4. Parameters Used for the Different LTV-MPC Configurations and PI Controller

Configuration	Parameters
Cfg-1- Longitudinal motion biased	$Q = \text{diag}[m^2 \;\; 10^{-7} \;\; 10^{-7} \;\; 10^{-7}]$ $\boldsymbol{r}_{\max} = [a_{x,\max} \;\; v_{x,\max} \;\; 0.7 \;\; 0.35]$ $\boldsymbol{r}_{\min} = [a_{x,\min} \;\; v_{x,\min} \;\; -0.7 \;\; -0.35]$
Cfg-2 Equal weighting	$Q = \text{diag}[m^2 \;\; 10^{-7} \;\; m^2 \;\; 10^{-7}]$ $\boldsymbol{r}_{\max} = [a_{x,\max} \;\; v_{x,\max} \;\; 0.5 \;\; 0.25]$ $\boldsymbol{r}_{\min} = [a_{x,\min} \;\; v_{x,\min} \;\; -0.5 \;\; -0.25]$
Cfg-3- Stability oriented	$Q = \text{diag}\,[\frac{m^2}{2} \;\; 10^{-7} \;\; I_{zz}^2 \;\; 10^{-7}]$ $\boldsymbol{r}_{\max} = [a_{x,\max} \;\; v_{x,\max} \;\; 0.3 \;\; 0.2]$ $\boldsymbol{r}_{\min} = [a_{x,\min} \;\; v_{x,\min} \;\; -0.3 \;\; -0.2]$
Cfg-AW-Adaptive weighting	$Q = \text{diag}\;(mg)^2\;[(\frac{w_{sc,a_x}}{2})^2\;(\frac{w_{sc,a_x}}{2})^2$ $(\frac{I_{zz}}{mg} w_{sc,\omega_z})^2\;(\frac{w_{sc,\beta}}{g})^2]$ $\boldsymbol{r}_{\max} = [a_{x,\min} \;\; v_{x,\min} \;\; \omega_{z,\max} \;\; \beta_{\max}]$ $\boldsymbol{r}_{\min} = [a_{x,\min} \;\; v_{x,\min} \;\; -\omega_{z,\min} \;\; \beta_{\min}]$
PI-Ctrl-Longitudinal control	$K_P = 4 \cdot m,\; K_I = 150$

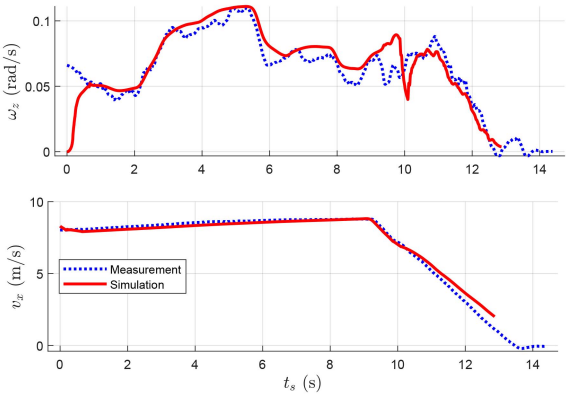

FIGURE 8. Sensor measurements from physical truck test (dotted black) using RT3000 [27] and simulation results obtained (orange) using replay of the measurement.

represent the vehicle configuration as in Fig. 2 and used to analyse different use cases.

V. RESULTS

The performance of the wheel torque coordination controller are evaluated using numerical simulations for different use cases. The simulations are performed in MATLAB/ Simulink environment using VTM vehicle plant model. The MPC parameter configurations presented in Table 5, including the adaptive tuning configuration were compared for the use cases. A proportional integral (PI) controller was also used as an alternative global force generator, for performance comparisons with the MPC. Since it is demanding to tune a multiple input multiple output system and guarantee feasible motion requests, only longitudinal force was requested using the PI controller. It was set to minimise the longitudinal acceleration

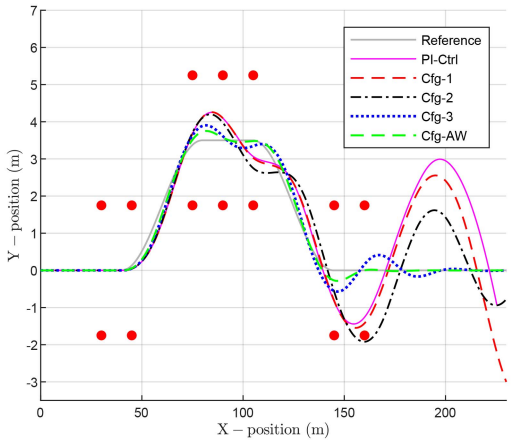

FIGURE 9. Vehicle CoG path profile on the road plane under the DLC test for the different MPC configurations.

error $e(t_s)$ from the driver model request to the vehicle performance.

$$\boldsymbol{v}_{\text{req}} = K_P \cdot e(t_s) + K_I \cdot \int_0^{t_s} e(\tau) d\tau \tag{34}$$

The PI controller error was tuned to match the MPC output with a gain for longitudinal force requests when not limited by constraints. Moreover, the force request $F_{x,req}$ was constrained using only the sum of all tyre force limits as in section 14 and not the actuator limits. The yaw moment request $M_{z,req}$ is excluded from the request interface to emulate a standard vehicle behaviour without any torque vectoring influence or intervention of a yaw stability controller.

The response of predicitive and PI controllers were analysed using both the open loop and closed loop (driver model in loop) use cases. In all the use cases, the MPC solver feasibility (when vehicle is not unstable) and convergence is ensured.

A. DOUBLE LANE CHANGE TEST

In this section, the vehicle's yaw response and stability characteristics are assessed using a double lane change (DLC) manoeuvre as shown in the Fig. 9. The vehicle follows a reference path between cones (red markers) at a speed of 15.28 m/s (55 km/h) and with a tire-road friction coefficient of 0.3.

Simulation results in the Fig. 9 shows the path traced by the vehicle's centre of gravity (CoG) across all the configurations. Notably, configuration Cfg-AW demonstrates superior agility and stability compared to other setups. It closely follows the reference path throughout the manoeuvre. Cfg-3, which emphasizes yaw rate error and tight lateral constraints, performs next best. In contrast, Cfg-1, Cfg-2, and PI-Ctrl show less agility, with significant deviations from the reference path, especially during the final phase of the manoeuvre ($120 - 180$ m). Cfg-1 and PI-Ctrl become unstable, whereas Cfg-2 remains somewhat more stable.

A deeper analysis, shown in Fig. 10, evaluates yaw rate, body side-slip angle, longitudinal acceleration, and steering

TABLE 5. Summary of Performance Achieved in Real World Driving Cycle for Different Configurations

Metrics used to evaluate configurations	Real world driving cycle					
	PI-Ctrl	Cfg-1	Cfg-2	Cfg-3	Cfg-AW	Cfg-AW-IL
Max. Distance from Center of lane, (m)	0.28	0.28	0.23	0.16	0.15	0.15
Max. Steering Wheel Angle (rad)	2.0	2.0	1.8	1.2	0.97	0.96
Total energy consumption (kWh)	1.20	1.20	1.19	1.18	1.18	1.18
Total Power consumed (kW)	$\bar{P}_{\text{cons}}$ = 44.8 σ_p= 19.3	$\bar{P}_{\text{cons}}$ = 44.9 σ_p= 19.4	$\bar{P}_{\text{cons}}$= 44.7 σ_p= 19.2	$\bar{P}_{\text{cons}}$= 44.5 σ_p= 19.1	$\bar{P}_{\text{cons}}$= 44.7 σ_p= 19	$\bar{P}_{\text{cons}}$= 34.1 σ_p= 19.5
Total longitudinal slip	$\bar{S}_x$= 0.004 σ_s= 0.003	$\bar{S}_x$ = 0.004 σ_s= 0.003	$\bar{S}_x$= 0.004 σ_s= 0.003	$\bar{S}_x$= 0.006 σ_s=0.004	$\bar{S}_x$= 0.007 σ_s= 0.006	$\bar{S}_x$= 0.006 σ_s= 0.004

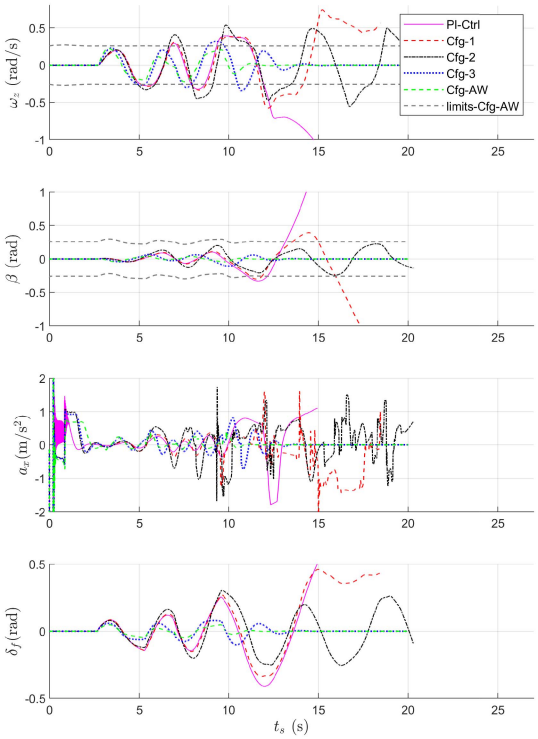

FIGURE 10. Vehicle state responses and front wheel steering inputs obtained from the vehicle plant for the DLC test. The grey dashed lines represent the limits from the Cfg-AW configuration.

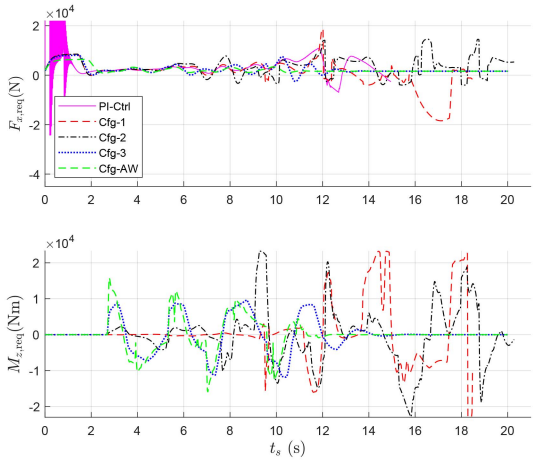

FIGURE 11. Longitudinal force and yaw moment requests requested by the global force reference generator across the configurations.

inputs. Cfg-AW maintains optimal performance throughout, followed by Cfg-3. During the initial phase ($\approx 2.5 - -4s$), all the configurations show sufficient agility, but Cfg-AW and Cfg-3 react more quickly. These configurations prioritize yaw moment requests over longitudinal forces, with Cfg-AW adapting requests dynamically. In the dwell phase ($\approx 4 - -5.5s$), both Cfg-AW and Cfg-3 maintain lower longitudinal force requests and generate higher yaw moments compared to Cfg-1 and Cfg-2. However, Cfg-AW exhibits more frequent changes in these requests, resulting in better lateral control and smaller deviations from the reference path. Cfg-1, Cfg-2, and PI-Ctrl exhibit higher overshoots in body slip β and yaw rate ω_z leading to increased lateral deviation. This behaviour corresponds with higher steering inputs and instability, particularly in Cfg-1 and PI-Ctrl. The responses of Cfg-1, Cfg-2 and PI-Ctrl, including a_x are amplified for the rest of manoeuvre leading to unstable vehicle behaviour. Interestingly, although Cfg-3 places higher priority and tighter constraints on ω_z and β, it still lags in performance when compared with Cfg-AW. These results highlights the need for dynamic weight balancing in the cost matrix Q and adapting the state constraints.

To analyse the vehicle's behavior, the controller output was examined, focusing on the force and moment requests generated by the global force reference generator and processed by the control allocator. Fig. 11 illustrates the global force requests during the manoeuvre, accounting for actuator limitations, tire force constraints, and vehicle motion states. As expected, each configuration follows distinct force request patterns: Cfg-1 prioritizes longitudinal force over yaw moment, while Cfg-2 generates moderate requests for both. In contrast, Cfg-3 and Cfg-AW prioritize yaw moment requests, with Cfg-AW adapting these requests dynamically during the manoeuvre.

a) During the initial phase ($2.5 - -4s$), the longitudinal force requests are similar across all configurations, including PI-Ctrl, with minor variations observed for Cfg-AW. However, Cfg-AW and Cfg-3 generate more pronounced yaw moment requests compared to other configurations, reducing lateral deviation from the reference path. Notably, Cfg-AW exhibits higher magnitudes of yaw moment requests, which change

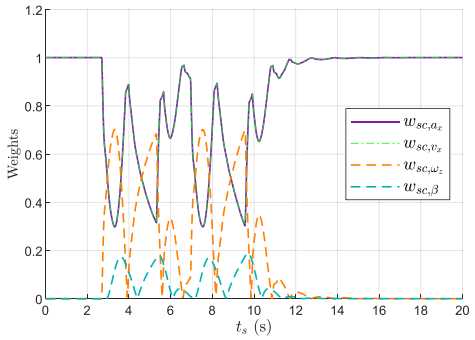

FIGURE 12. Variation of normalized weights for Cfg-AW during the DLC manoeuvre.

more rapidly than in Cfg-3, contributing to better path tracking.

b) In the dwell phase ($4 - -5.5s$), longitudinal force requests in Cfg-AW and Cfg-3 remain lower than in Cfg-1 and Cfg-2, with both configurations generating larger yaw moment requests. Due to its adaptive limits, Cfg-AW exhibits more frequent changes in these requests compared to Cfg-3. This rapid adaptation reduces deviations from the reference path, as observed in Fig. 9. In contrast, Cfg-1 and Cfg-2 become less effective, resulting in higher lateral deviations and increased steering wheel input to compensate for the error.

c) For the remainder of manoeuvre ($5.5 - 10.5s$), Cfg-AW continues to request smaller, stable longitudinal forces. As a result, the vehicle states (ω_z and β) remain within defined limits. Conversely, longitudinal force requests for Cfg-1 and Cfg-2 increase over time, leading to yaw rate overshoots and lower yaw moment requests $M_{z,\text{req}}$, which peak around $9 - -10\ s$, especially in Cfg-2. This increase in longitudinal force leads to greater lateral deviation and higher steering inputs, contributing to instability, particularly in the terminal phase.

The global force reference generator outputs are directly related to the adaptive state cost weighting, as shown in Fig. 12. The evolution of normalized weights and their relation to global force requests depends on the proximity of the vehicle's lateral states (ω_z and β) to their limits. When these lateral states approach their defined limits, the controller reduces the weights associated with longitudinal states and vice versa. Notably, the weight $w_{sc,\beta}$ associated with the body side-slip angle does not directly affect the vehicle's slip angle but is indirectly controlled through the longitudinal state weight w_{sc,a_x} as specified in (28). This adaptive tuning approach is a proof of concept, with simple relationships defined that could be further refined with additional states and more complex interrelations.

Fig. 13 illustrates how the global force requests are processed by the control allocator and converted into individual wheel torque commands. During the active phase of the manoeuvre ($2.5 - 10.5s$), configurations Cfg-AW and Cfg-3 effectively achieve the desired yaw moment by generating differential wheel torques. This targeted distribution enhances yaw control and contributes to improved stability. In contrast, Cfg-1 and Cfg-2 exhibit significant differential torques primarily during the terminal phase, accompanied by larger steering angle inputs. Notably, in Cfg-1, negative torque levels increase toward the end of the manoeuvre, with ABS activation observed from around $12s$ especially on the rear axle. This results in oversteering tendencies and aligns with the observed increase in body slip angle (β),, confirming instability. As expected, PI-Ctrl shows minimal torque differentiation between the left and right wheels, indicating no active yaw moment generation. These findings underscore the benefits of adaptive control—particularly in Cfg-AW—in enforcing constraints and distributing control effort effectively. The ability to modulate force requests and translate them into precise actuator commands is crucial for maintaining vehicle stability and agility under high-demand scenarios.

B. DRIVING IN A SPLIT-μ CURVE

To evaluate the driver assistance capability of the wheel torque controller configurations, manoeuvring a curve with split friction was evaluated. The use case was carried out on a curve with a radius of 115 m, a constant vehicle speed of 60 km/h and friction on the left side as $\mu_{lh} = \mu = 0.2$ and that on the right side as $\mu_{rh} = 3\mu$. To have a stable vehicle behaviour and perform uniform analysis, the split-μ road condition started after 5 s into the simulation corresponding to ≈ 80 m. The performance was analysed by observing the lateral vehicle deviation and driver steering wheel angle input required for the different configurations.

Fig. 14 shows the path tracked by the vehicle CoG for all the configurations. The results show that Cfg-AW tracked the intended path with lowest magnitude of the lateral deviation and the steering wheel input for the entire manoeuvre. As expected, the configurations PI-Ctrl and Cfg-1, with higher weights prioritising the state $\dot{v}_x$ over ω_z, is very poor in lateral tracking of the intended path and correspondingly the steering wheel angle input. However, observing the results, the performance is poorer only during the initial phase of manoeuvre (≤ 105 m). During the later phase, performances of Cfg-2 and Cfg-3 are seen to be poorer and the vehicle becomes unstable in case of Cfg-3. These results were completely unexpected especially when compared to the results from DLC use case. With the relatively high prioritisation of yaw rate tracking, one would have expected a more stable and improved performance than Cfg-1 and PI-Ctrl. The performance metrics for the use case are presented in Fig. 15. The lateral deviations are significant in the case of Cfg-1 and PI-Ctrl during the initial phase and subside over the distance travelled. With equal and higher weighting of the lateral states compared to longitudinal states, improved performance is achieved in the case of Cfg-2 and Cfg-3, respectively. However, as stated earlier the performance became worse in the later phase of the manoeuvre, which was unexpected. In contrast, Cfg-AW which adapts the longitudinal and lateral state related weights shows the most promising results. Thus setting constant weights and tuning

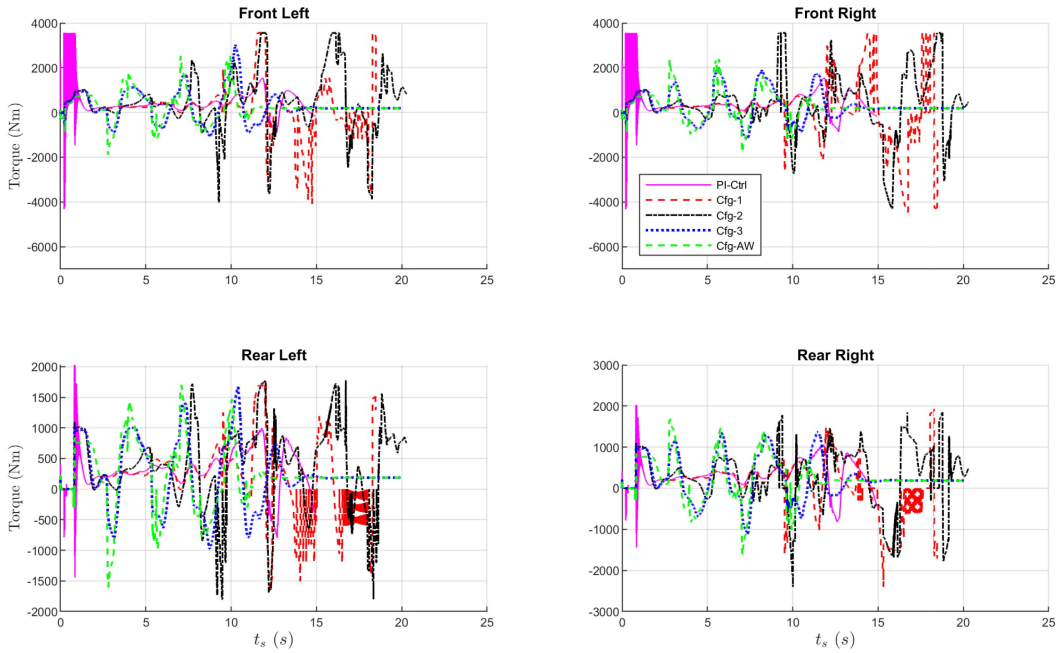

FIGURE 13. Wheel torques requests across all the configurations for the DLC use case.

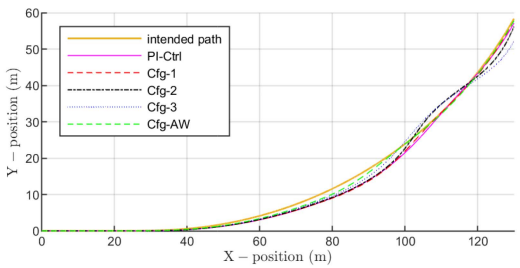

FIGURE 14. Vehicle CoG path followed for the split- μ driving in a curve.

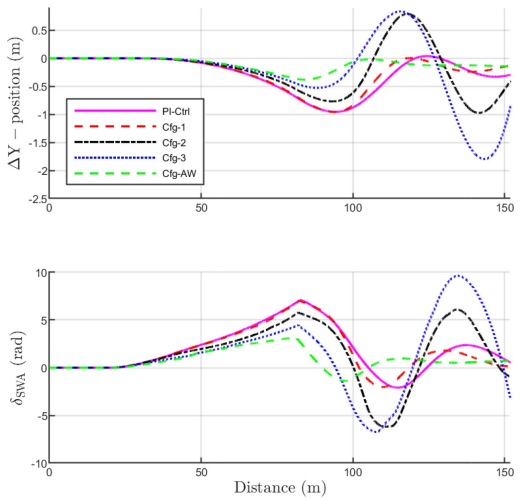

FIGURE 15. Lateral deviation of the CoG from the intended path and steering wheel angle response by the driver over distance travelled during the split-μ drive in a curve manoeuvre.

for a specific use case may not be optimal for other cases, as seen in the case of Cfg-2 and Cfg-3.

To understand the influence of the controller tuning on vehicle performance, the vehicle states in Fig. 16 and the global force requests in Fig. 17, are analysed. Due to its superior performance, the Cfg-AW was used as a reference compared with other configurations. Before encountering the split-μ conditions (around 5 s) some differences were observed when entering and negotiating the curve. PI-Ctrl without additional and Cfg-1 with delayed yaw moment requests respectively, relied on the steering inputs from the driver model leading to increased steering wheel angle input and also lateral deviation. The level of these inputs generated a lower body slip angle and yaw rate when compared with Cfg-2 and Cfg-3. In the case of Cfg-2 and Cfg-3, a high yaw rate and body slip angle were observed due to the relatively higher yaw moment and longitudinal force requests before approaching split-μ conditions. These requests were generated on the basis of constant parameters state limits and state costs, which could be excessive or insufficient depending on the vehicle state and driving scenario. Meanwhile, Cfg-AW with adaptive tuning of parameters was observed to regulate the longitudinal force and yaw moment requests ($2.5 - 5\ s$), thereby attempting to keep β and ω_z within the limits.

Finally, when split-μ conditions are active, significant yaw moment was requested along with the longitudinal force requests in the case of Cfg-2, Cfg-3 and Cfg-AW. Cfg-AW with adaptive state limits and state costs, continuously varied the global force requests, altering the vehicle states and keeping the vehicle stable. However, in the case of Cfg-2 and Cfg-3 entering with high β and ω_z, along with constant parameters

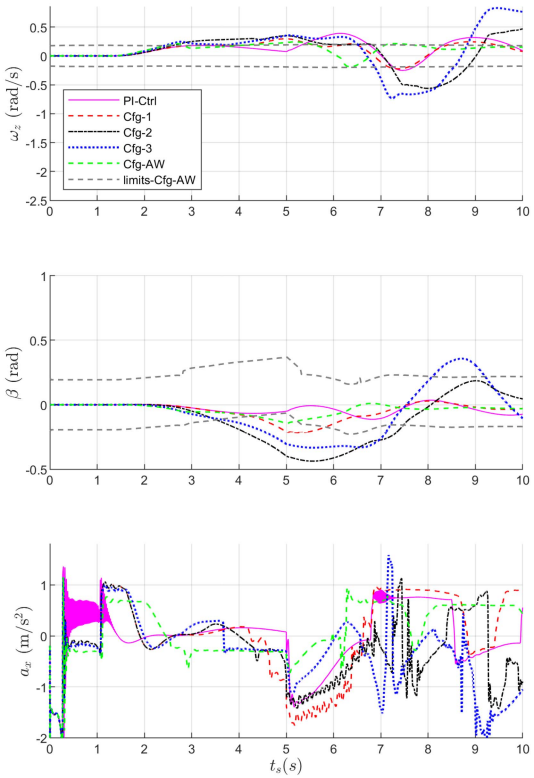

FIGURE 16. Vehicle state responses for the split-μ drive in a curve use case for the different MPC configurations.

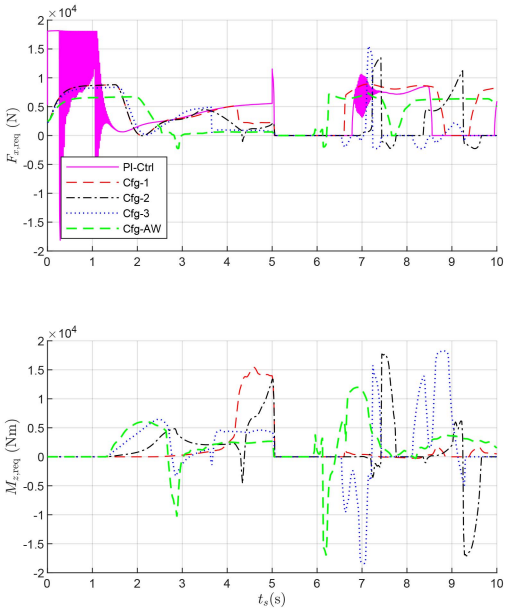

FIGURE 17. Longitudinal force and yaw moment requests by the global force reference generator.

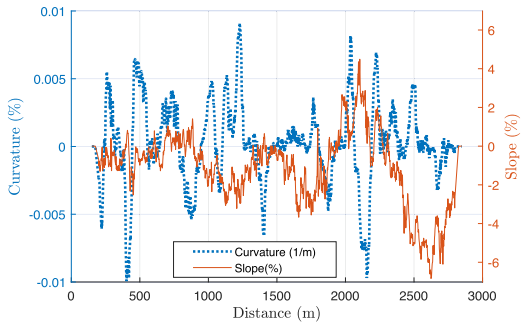

FIGURE 18. Road curvature and slope for the real world driving cycle use case.

of the state limits and uncoupled state costs, produce proportional global force requests. Such force requests exceed the desired value leading to overshoots in ω_z or β and unstable vehicle behaviour. In the case of Cfg-1 and PI-Ctrl with longitudinal force prioritisation, the lateral deviations and steering wheel angle are seen to damp over time with the help of driver corrections. Hence, these results highlight that adapting the MPC's state limits and weights of state costs is important to achieve the desired and stable vehicle performance.

C. REAL WORLD DRIVING CYCLE

To analyse the robustness of parameters and adaptive tuning of weights used in the MPC configurations a portion of a real world driving cycle with critical road conditions was used to complement the short duration and dynamic use cases. The goal was also verify the energy efficiency, stability and driver effort metrics of the configurations including an additional configuration Cfg-AW-IL. In Cfg-AW-IL, which used the same adaptive weights as Cfg-AW, the principle of power loss minimization including idle losses is implemented. For the driving cycle it is also observed that the IM is not active for the entire driving cycle.

The test was performed on a rural road segment between Hällered and Alingsås, which are two villages in western Sweden, for approximately 2.7km. This test assumes that a driver is driving slightly above normal speed at 65 km/h on a winter road with a friction coefficient of 0.4. The driving cycle was simulated under standard winter conditions with varying road curvature, camber, road profile and slope. Fig. 18 shows the minimum applicable description of the driving cycle. The simulation results show that all the configurations successfully completed the entire driving cycle and no differences are seen in the simulation time of $\approx$ 150 s.

Fig. 19 compares the lateral deviation and steering angle input for the defined use case across the configurations. As from the results for the previous use cases, the configuration Cfg-AW and Cfg-AW-IL outperforms the other configurations with Cfg-1 and PI-Ctrl with the satisfactory performances. Noticeably, Cfg-AW-IL has very similar performance levels as Cfg-AW and are nearly half the magnitudes compared with Cfg-1 and PI-Ctrl. Performance of Cfg-2 and Cfg-3, lies is between Cfg-1 and Cfg-AW, with Cfg-3 producing lower magnitude of the lateral deviation and steering angle input than Cfg-2. The summary of the performance for comparison among configurations are presented in the Table 5.

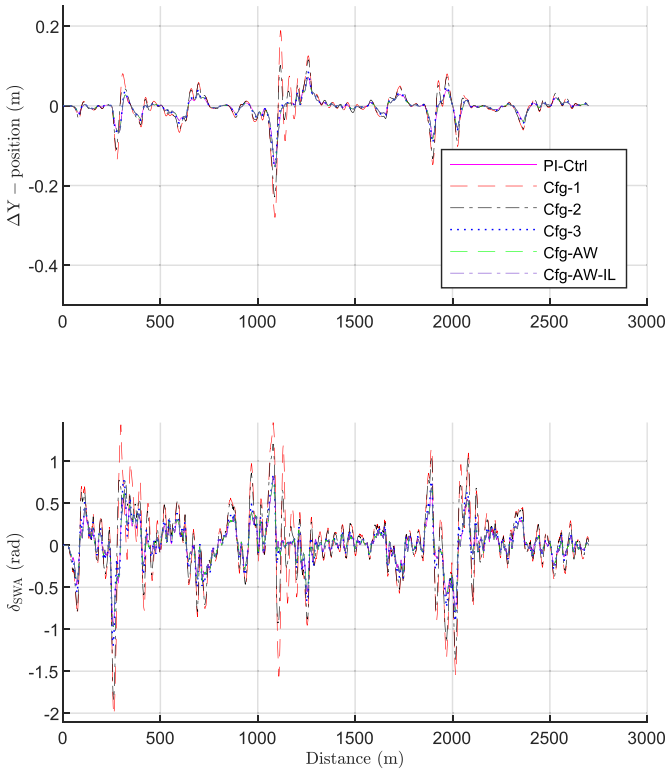

FIGURE 19. Lateral deviation from the centre of lane and steering wheel angle input from the driver model for a real-world driving cycle under winter conditions and with a constant speed of 65 km/h.

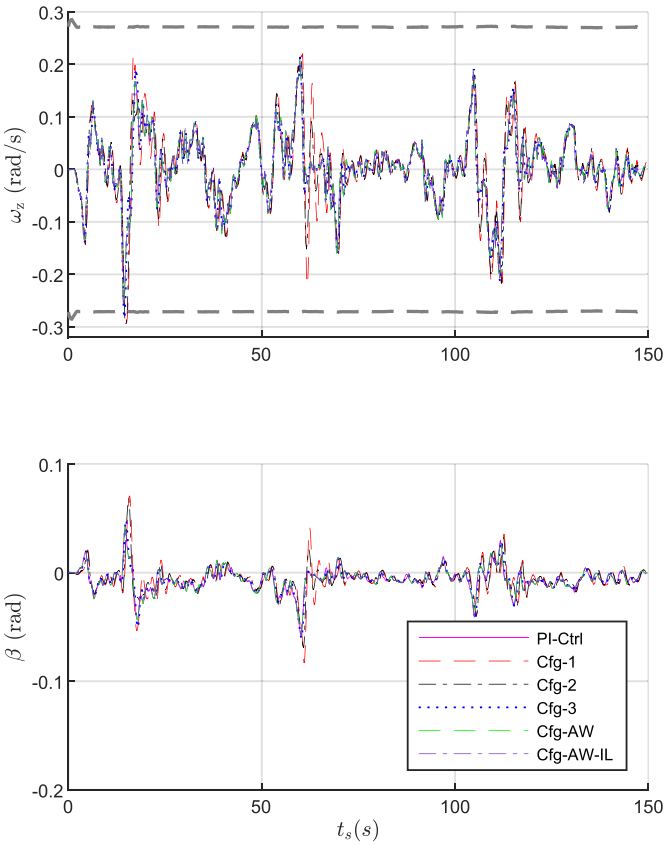

FIGURE 20. Yaw rate and body side slip angle across the configurations with the grey dashed lines representing the limits for $\omega_{z,max}$ and $\omega_{z,min}$.

The magnitude of the lateral vehicle states ω_z and β for the configurations are all within the dynamic limits obtained from Cfg-AW as seen in Fig. 20. Hence, no unstable vehicle behaviour is observed on the specified real world driving cycle across the configurations.

Finally, the importance of considering idle losses and their impact on energy consumption is presented in the Table 5. The results highlight the total energy consumed, mean power consumption $\bar{P}_{\text{cons}}$ with the standard deviation σ_p, and the total longitudinal slip on all four wheels $\bar{S}_x$ with standard deviation σ_s for entire the driving cycle. As clearly evident from the results, the configuration Cfg-AW-IL reduces the total power consumption, due to reduction of idle losses of the IM on the startability axle. The remaining configurations show no significant differences in power consumption. The impact of such a lower power consumption is minimal considering the short driving cycle and hence no major difference is seen between Cfg-AW and Cfg-AW-IL for the total energy consumed over time. Additionally, no significant differences are seen in case of $\bar{S}_x$ among the configurations. As only the front axle is propelled predominantly in case of Cfg-AW-IL compared to Cfg-AW, one would have expected higher slip values. However, for the given vehicle configuration with high normal load on the front axle and the absence of slip on the rear axle lowers the overall slip magnitude in favour of Cfg-AW-IL. This highlights the importance of observing load distribution for different applications when configuring drivetrains across the axles. Although Cfg-AW-IL results in reduced energy consumption and low slip values, one should be vary of the stability related issues by propelling on a single axle especially on low friction road conditions. These findings corroborate the claim that the proposed axle coordination controller with adaptive weight tuning help to significantly improve vehicle performance and energy efficiency on real world driving cycles too.

VI. CONCLUSION

In this article, a hierarchical axle torque coordination framework for heavy vehicles with multiple electric drivetrains is proposed. The axle torque coordination controller converted motion request into energy efficient wheel torque requests while ensuring safe operation. A linear time varying MPC scheme that continuously adapts the cost weights in the objective function and state limits in the predictive controller was proposed. The longitudinal force and yaw moment request from MPC scheme are coordinated instantaneously by a control allocator to the actuators while minimizing power losses of the actuators. An alternate method to consider idle losses of the induction machines in the control allocator is also proposed. Different configurations of fixed state cost weights

and state limits were compared with the adaptive configuration. Simulations were performed using a high fidelity vehicle model, which was validated using real test measurements for winter conditions.

Results from the use cases demonstrate that the wheel torque coordination framework with adaptive tuning of state cost weights significantly improves the vehicle performance and energy efficiency while reducing driver effort. In particular, the results of the DLC test clearly show that varying longitudinal and lateral weights simultaneously improves vehicle agility, maintains vehicle stability and achieves predictive performance. For the split-μ in curve use case, the driver effort and the lateral deviation is significantly reduced. Lastly, for the real-world driving cycle use case, the configuration with adaptive tuning achieved the optimal performance. An energy efficiency improvement of 1% is seen between Cfg-1 and Cfg-AW / Cfg-AW-IL configuration for such a short driving cycle. Favourable improvements are also seen with configuration considering idle losses while being stable.

For future works, verification of the MPC tuning for different vehicle configurations will be beneficial to validate the adaptive tuning concept. Further investigations into the robustness of model uncertainties and computational efficiency is needed to refine and develop the framework. Analysis of different axle-usage modes in the case of actuator failures will also benefit the research.

REFERENCES

[1] International Energy Agency, "Trends in electric heavy-duty vehicles," 2025. Accessed: Apr. 8, 2025. [Online]. Available:https://www.iea.org/reports/global-ev-outlook-2024/trends-in-heavy-electric-vehicles

[2] M. Haghani, F. Sprei, K. Kazemzadeh, Z. Shahhoseini, and J. Aghaei, "Trends in electric vehicles research," *Transp. Res. Part D: Transport Environ.*, vol. 123, 2023, Art. no. 103881. [Online]. Available: https://www.sciencedirect.com/science/article/pii/S136192092300278X

[3] L. D. Novellis, A. Sorniotti, and P. Gruber, "Design and comparison of the handling performance of different electric vehicle layouts," *Proc. Inst. Mech. Engineers, Part D: J. Automobile Eng.*, vol. 228, no. 2, pp. 218–232, 2014. [Online]. Available: https://doi.org/10.1177/0954407013506569

[4] M. Asperti, M. Vignati, and E. Sabbioni, "On torque vectoring control: Review and comparison of state-of-the-art approaches," *Machines*, vol. 12, no. 3, 2024, Art. no. 160. [Online]. Available: https://www.mdpi.com/2075-1702/12/3/160

[5] C. Chatzikomis et al., "An energy-efficient torque-vectoring algorithm for electric vehicles with multiple motors," *Mech. Syst. Signal Process.*, vol. 128, pp. 655–673, 2019. [Online]. Available: https://www.sciencedirect.com/science/article/pii/S0888327019301657

[6] A. Wong, D. Kasinathan, A. Khajepour, S.-K. Chen, and B. Litkouhi, "Integrated torque vectoring and power management framework for electric vehicles," *Control Eng. Pract.*, vol. 48, pp. 22–36, 2016. [Online]. Available: https://www.sciencedirect.com/science/article/pii/S0967066115300587

[7] J. Liang et al., "An energy-oriented torque-vector control framework for distributed drive electric vehicles," *IEEE Trans. Transport. Electrific.*, vol. 9, no. 3, pp. 4014–4031, 2023.

[8] H. Peng, W. Wang, C. Xiang, L. Li, and X. Wang, "Torque coordinated control of four in-wheel motor independent-drive vehicles with consideration of the safety and economy," *IEEE Trans. Veh. Technol.*, vol. 68, no. 10, pp. 9604–9618, Oct. 2019.

[9] H. Zhang et al., "An energy efficient control strategy for electric vehicle driven by in-wheel-motors based on discrete adaptive sliding mode control," *Chin. J. Mech. Eng.*, vol. 36, no. 1, 2023, Art. no. 58. [Online]. Available: https://doi.org/10.1186/s10033-023-00878-6

[10] S. Yue and Y. Fan, "Hierarchical direct yaw-moment control system design for in-wheel motor driven electric vehicle," *Int. J. Automot. Technol.*, vol. 19, no. 4, pp. 695–703, 2018.

[11] X. Hu, P. Wang, Y. Hu, and H. Chen, "A stability-guaranteed and energy-conserving torque distribution strategy for electric vehicles under extreme conditions," *Appl. Energy*, vol. 259, 2020, Art. no. 114162. [Online]. Available: https://www.sciencedirect.com/science/article/pii/S0306261919318495

[12] Q. Kang, D. Meng, Y. Jiang, C. Zhao, H. Chu, and B. Gao, "Torque vectoring control of distributed drive electric vehicles using fast iterative model predictive control," *IFAC-PapersOnLine*, vol. 58, no. 29, pp. 106–111, 2024. [Online]. Available: https://www.sciencedirect.com/science/article/pii/S2405896324022699

[13] A. Parra, D. Tavernini, P. Gruber, A. Sorniotti, A. Zubizarreta, and J. Pérez, "On nonlinear model predictive control for energy-efficient torque-vectoring," *IEEE Trans. Veh. Technol.*, vol. 70, no. 1, pp. 173–188, 2021.

[14] N. Guo, X. Zhang, Y. Zou, B. Lenzo, T. Zhang, and D. Göhlich, "A fast model predictive control allocation of distributed drive electric vehicles for tire slip energy saving with stability constraints," *Control Eng. Pract.*, vol. 102, 2020, Art. no. 104554. [Online]. Available: https://www.sciencedirect.com/science/article/pii/S0967066120301519

[15] N. Guo et al., "Handling-stability control for distributed drive electric vehicles via lyapunov-based nonlinear MPC algorithm," *IEEE Trans. Transport. Electrific.*, vol. 11, no. 2, pp. 6615–6628, Apr. 2025.

[16] H. Yin, C. Ma, H. Wang, Z. Sun, and K. Yang, "Optimal driving torque control strategy for front and rear independently driven electric vehicles based on online real-time model predictive control," *World Electric Veh. J.*, vol. 15, no. 11, 2024, Art. no. 533. [Online]. Available: https://www.mdpi.com/2032-6653/15/11/533

[17] N. Guo, J. Ye, and Z. Huang, "Cooperative control of distributed drive electric vehicles for handling, stability, and energy efficiency, via ars and dyc," *Sustainability*, vol. 16, no. 24, 2024, Art. no. p11301. [Online]. Available: https://www.mdpi.com/2071-1050/16/24/11301

[18] W. Wang, J. Li, X. Li, Z. Li, and N. Guo, "Multi-objective collaborative control method for multi-axle distributed vehicle assisted driving," *Appl. Sci.*, vol. 13, no. 13, 2023, Art. no. 7769. [Online]. Available: https://www.mdpi.com/2076-3417/13/13/7769

[19] N. Guo, X. Zhang, Y. Zou, B. Lenzo, G. Du, and T. Zhang, "A supervisory control strategy of distributed drive electric vehicles for coordinating handling, lateral stability, and energy efficiency," *IEEE Trans. Transport. Electrific.*, vol. 7, no. 4, pp. 2488–2504, Dec. 2021.

[20] Fröjd N., "Handling analysis and control development of commercial trucks with volvo transport models," 2024. Accessed: Oct. 05, 2024. [Online]. Available: https://se.mathworks.com/videos/handling-analysis-and-control-development-of-commercial-trucks-with-volvo-transport-models-1622035211192.html

[21] S. Janardhanan, "On power loss minimisation for heavy vehicles with axle-wise and modular electrical propulsion and friction braking," Licentiate Thesis, Chalmer Univ. of Technology, Göteborg, Sweden, Feb. 2023.

[22] J. Persson and J. Åkesson, "On torque vectoring to improve steering predictability while minimising power loss in heavy electric vehicles using model predictive control," Master's Thesis, Chalmers Univ. Technol., Göteborg, Sweden, 2022. [Online]. Available: https://hvttforum.org/wp-content/uploads/2023/12/HVTT17_paper_3004_Erdinc.pdf

[23] U. Erdinc, M. Jonasson, M. S. Kati, B. J. H. Jacobson, J. Fredriksson, and L. Laine, "Modelling of articulated heavy vehicles for computation of accurate safe operating envelope for yaw stability," in *Proc. 17th Int. Symp. Heavy Veh. Transport Technol.* vol. 17, Brisbane, Australia, 2023.

[24] C. G. Bobier, "A phase portrait approach to vehicle stabilization and envelope control," Ph.D. Dissertation, Stanford Univ., Stanford, CA, USA, 2012.

[25] G. De Filippis, B. Lenzo, A. Sorniotti, P. Gruber, and W. De Nijs, "Energy-efficient torque-vectoring control of electric vehicles with multiple drivetrains," *IEEE Trans. Veh. Technol.*, vol. 67, no. 6, pp. 4702–4715, Jun. 2018.

[26] S. Janardhanan, L. Henderson, M. Jonasson, B. Jacobson, and E. R. Gelso, "Simulation-based assessment of wheel torque allocation strategies on heavy vehicles with drivetrains on multiple axles," *Transp. Eng.*, vol. 20, 2025, Art. no. 100322. [Online]. Available: https://www.sciencedirect.com/science/article/pii/S2666691X25000223

[27] O. Ltd, "RT3000 v4: Inertial navigation solution," 2025. Accessed: Sep. 15, 2025. [Online]. Available: https://www.oxts.com/solutions/inertial-navigation-solutions/navigation-hardware/rt3000-v4/